Inferring the relationship between core-mantle heat flux and seismic tomography from mantle convection simulations

G. Choblet [a],[*], F. Deschamps [b], H. Amit [a], M. Lasbleis [a]

[a] *Nantes Université, Univ Angers, Le Mans Université, CNRS, UMR 6112, Laboratoire de Planétologie et Géosciences, F-44000 Nantes, France*
[b] *Institute of Earth Sciences, Academia Sinica, 128 Academia Road, Section 2, Nangang, Taipei 11529, Taiwan*

A R T I C L E   I N F O

A B S T R A C T

The heat flux pattern at Earth's core-mantle boundary (CMB) imposes a heterogeneous boundary condition on core dynamics that may profoundly affect the geodynamo. Owing to the expected temperature dependence of seismic velocities, this pattern is classically approximated as proportional to the lowermost layer of seismic tomography models for the global mantle. Two biases however undermine such a simple linear relationship: 1) other contributions than thermal (compositional and mineralogical) influence seismic velocities and 2) the radial average is inherent to tomographic models whereas the local thermal state at the CMB is relevant for the heat flux. We analyze here simulations of thermochemical mantle convection where, owing to their spatial characteristics, specific mantle components are readily identified: hot thermochemical piles (TCPs), "normal" mantle (NM) and, when post-peroskite (pPv) is included, a cold region where this phase is present. Synthetic seismic velocities (i.e. from the mantle simulations) are then computed based on thermal, compositional and mineralogical sensitivities. A formalism to infer the CMB heat flux from these seismic shear velocity anomalies is derived. In this formalism, within each mantle population (i.e. TCPs, NM or pPv) the CMB heat flux vs. seismic anomalies follows a unique fitting function. The transition from one mantle population to another is marked by a jump in the seismic anomaly, i.e. a range of seismic anomalies in between two mantle populations corresponds to a similar CMB heat flux. Applying our formalism to the seismic anomalies from the mantle convection simulations provides far superior fits than the commonly used linear fits. The results highlight reduced negative heat flux anomalies beneath large low shear velocity provinces (LLSVPs), while positive heat flux anomalies are enhanced, both with respect to the classical linear interpretation.

1. Introduction

The heat flowing through the Earth's core-mantle boundary (CMB) results from the mantle's ability to transfer this heat to the planet's surface. Globally, the evolution and present-day value of its magnitude control the thermal state of the lowermost mantle (see Lay et al., 2008; Hernlund and McNamara, 2015, for syntheses). Related important questions include: do patches at the bottom of the mantle remain partially molten at present? Does post-perovskite (pPv) exist above the CMB and, if yes, how is it distributed? The global heat power through the CMB also largely affects the core dynamics as the dominant provider of buoyancy, either because it permits cooling of the liquid core, or because it enables the inner core growth (e.g. Christensen and Aubert, 2006; Olson et al., 2015). At present, whether CMB heat flux is superadiabatic or not dictates if a stable region of thermal origin occupies the top of the

liquid core (Kaneshima, 2018; Irving et al., 2018).

While the amount of heat extracted globally by the mantle remains uncertain, lateral variations of heat flux are anticipated as a natural outcome of mantle convective dynamics. Mantle tomography models confirm that cold material, such as subducting slabs, is adjacent to presumably hotter regions associated with hot rising plumes beneath the Pacific and Africa (e.g. Lekic et al., 2012; Cottaar and Lekic, 2016). The pattern of CMB heat flux also has important consequences for core dynamics and the geomagnetic field (Amit et al., 2015a). Numerical dynamo models with heterogeneous outer boundary heat flux demonstrated that the locations of positive heat flux anomalies determine preferred sites of outer core fluid downwellings that concentrate intense geomagnetic flux patches (e.g. Olson and Christensen, 2002; Gubbins et al., 2007; Sahoo and Sreenivasan, 2020). Likewise, negative heat flux anomalies lead to outer core fluid upwellings that disperse

---

* Corresponding author.
E-mail address: gael.choblet@univ-nantes.fr (G. Choblet).

Table 1
Setups and some generic results of the six simulations used in this study. The values of the two specific parameters varied among these models are the dimensionless activation energy E_a controlling the temperature-dependence of mantle viscosity and the Clapeyron slope considered for the phase transition from bridgmanite to post-perovskite. $< T >$ is the averaged mantle temperature. F_t and F_b are the mean top and bottom heat fluxes, σ_{F_b} is the standard deviation of the latter. D18 refers to Deschamps et al. (2018).

case	E_a	pPv?	Clapeyron (MPa K^{-1})	label in D18	$< T >$ (K)	F_t (mW m^{-2})	F_b (mW m^{-2})	σ_{F_b} (mW m^{-2})
A	20.7	no	–	TC1	1830	34.1	54.8	63.1
B	13.8	no	–	TC2	1410	35.2	67.2	55.1
C	20.7	single crossing	8	–	1960	40.8	90.7	61.3
D	13.8	double crossing	13	TC2-pPv	1820	62.4	127.8	93.7
E	20.7	double crossing	13	TC1-pPv	2090	48.5	114.6	99.1
F	20.7	double crossing	16	–	2120	48.3	119.6	111.8

geomagnetic flux (Terra-Nova et al., 2016) and may result in surface intensity minima as observed nowadays in the South Atlantic (Tarduno et al., 2015; Terra-Nova et al., 2019). Low-latitude intense geomagnetic flux patches, which are usually absent in dynamo models with homogeneous boundary conditions, may be driven by a specific CMB heat flux pattern (Amit et al., 2015b). The geomagnetic secular variation, in particular the hemispheric dichotomy between the active Atlantic to the quiet Pacific, may also be affected by CMB heat flux heterogeneity (Christensen and Olson, 2003). If the CMB driven flow extends along axial columns (as expected in a rapidly rotating system) across the outer core to the inner core boundary, then lower mantle heterogeneity may prescribe preferred sites of inner core growth (Aubert et al., 2008; Gubbins et al., 2011). On much longer timescales, CMB heat flux heterogeneity may control the frequency of paleomagnetic reversals (e.g. Glatzmaier et al., 1999; Kutzner and Christensen, 2004; Olson et al., 2010; Choblet et al., 2016), in particular the onset and termination of superchrons (Biggin et al., 2012; Olson et al., 2015; Yoshimura, 2022). All these observed geodynamo features are potentially controlled by lower mantle heterogeneity and hence require precise knowledge of the CMB heat flux pattern.

In principle, access to the CMB heat flux pattern may be provided by the lowest layer of mantle tomography models. Inferring the thermal state immediately above the CMB from seismic velocity anomalies (averaged over typically 100–200 km above the CMB) can however be challenged by two biases: (1) other sources than thermal may contribute to the tomographic pattern, and (2) radial temperature gradients are large in this region, so that a radial average might blur the CMB pattern. While, to our knowledge, problem (2) has never been adequately addressed, problem (1) is recognized as a classical issue for this exercise: the deepest mantle is indeed considered as a deep mirror of the lithospheric region where compositional and mineralogical complexities also prevail. Several hints, including the anti-correlation between shear and bulk sound velocities (Ishii and Tromp, 1999; Masters et al., 2000; Trampert et al., 2004; Houser et al., 2008), estimates of lateral variations in density (Trampert et al., 2004; Mosca et al., 2012; Moulik and Ekström, 2016), tidal tomography (Lau et al., 2017), attenuation measurements (Deschamps et al., 2019) and the 6-years variations in the length-of-the-day (Ding and Chao, 2018), all point to the presence of large-scale variations in lowermost mantle composition, with possible enrichment in iron in regions associated with low shear velocity (Trampert et al., 2004; Deschamps et al., 2012). Attempts at identifying the thermal contribution to seismic velocity anomalies have been suggested: Hernlund and McNamara (2015) proposed a CMB heat flux map based on P-wave velocity inspired by the notion that these are less affected than S-waves by changes in composition and the presence of pPv. P-wave tomography models are however less precise and the P-wave counterparts of LLSVPs are weaker. In addition, the consensus among P-wave tomography models is less pronounced for the lowermost mantle (Cottaar and Lekic, 2016) than the consensus among S-wave models (Lekic et al., 2012). Amit et al. (2015b) used the thermal component of a probabilistic tomography model that seeks to

independently constrain density and seismic velocity anomalies by including normal mode data in the seismic data set (Mosca et al., 2012). To provide a better mapping of CMB heat flux, we note however that normal mode tomography models may need further developments, in particular improved spatial resolution and a better treatment of mode coupling to determine structure coefficients (e.g. Yang and Tromp, 2015).

An alternative approach is to guide the interpretation of mantle tomography by insights gained from mantle convection models. This assumes that the latter provide dynamical constraints on the various mantle components whose compositional or mineralogical characteristics affect seismic velocities. Nakagawa and Tackley (2008) computed synthetic shear velocity anomalies from mantle convection simulations, at a significant distance ($\simeq 150$ km) from the CMB and compared these to the CMB heat flux. The present study is largely inspired by this approach. Amit and Choblet (2009) used such results to interpret tomography models in the presence of pPv. Amit and Choblet (2012) envisioned that specific small-scale thermal anomalies might not be resolved by tomographic models and studied their effect. Overall, the CMB heat flux maps derived in such studies were found to provide either modest changes that weakly affect the geodynamo (Amit and Choblet, 2009, 2012) or dramatic modifications when probabilistic tomography models are used (Amit et al., 2015b).

Here, we propose to analyze mantle convection simulations that include the effect of composition and phase-change in order to interpret the shear velocity (V^s) anomalies derived by global tomographic models. A specific focus on the typical radial resolution ($\simeq 200$ km) of global mantle tomography models (Problem 2 above) is proposed: we consider the 200-km thick bottom layer of state-of-the-art mantle convection simulations for the lowermost mantle (Deschamps et al., 2018) and propose an algorithm to convert V^s anomalies (an average over this 200-km thick layer) into heat flux Q_{cmb} anomalies (a local value at the CMB). Section 2 describes the mantle convection simulations, the relationship used to compute synthetic V^s anomalies from these simulations as well as the principle of our approach. The results are described and analyzed in Section 3. An algorithm relating V^s and Q_{cmb} is proposed and its applicability discussed in Section 4.

2. Methods

In this section, we describe the method used to compute synthetic seismic velocities and CMB heat flux from the mantle simulations. These distributions are derived from thermal, compositional and phase fields obtained by numerical simulations of thermochemical convection. Seismic velocity anomalies further require the prescription of seismic sensitivities deduced from mineral physics data and equation of state modeling. We then describe the method to relate seismic and thermal anomalies in the mantle convection simulations.
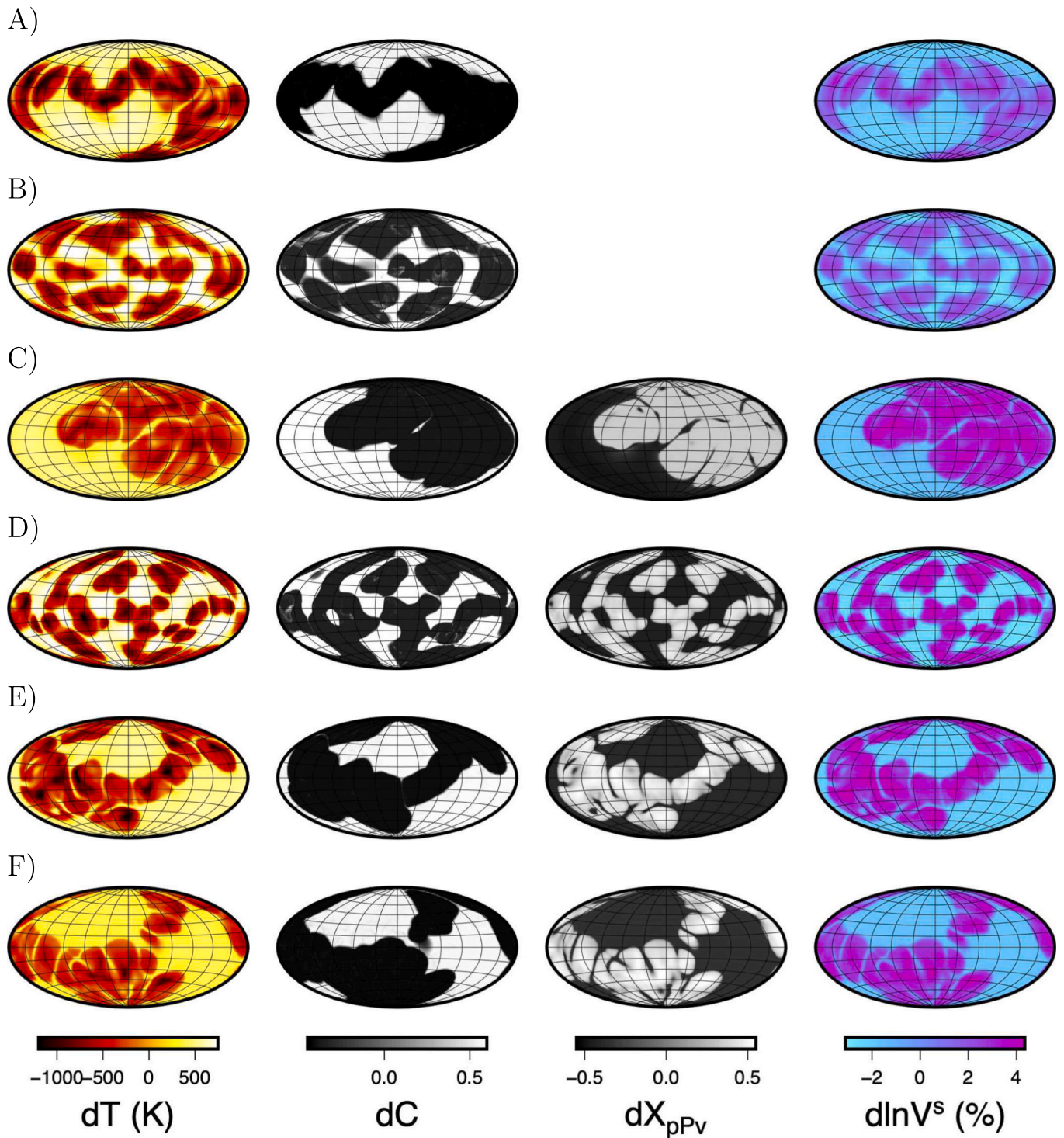
Fig. 1. Patterns of anomalies for the various fields (temperature T, composition C and, when pertinent, fraction of post-perovskite X_{pPv}) as well as the resulting seismic shear velocities (V^s) above the CMB for the six simulations (A to F). The fields are averaged in a 200 km-thick layer above the bottom boundary of the simulations.

2.1. Mantle convection simulations

The thermal, compositional and phase fields used to calculate synthetic seismic velocity anomalies and bottom heat flux are snapshots taken from six simulations of mantle thermochemical convection, some of these already presented in Deschamps et al. (2018). The models setups and some generic results are listed in Table 1. In order to assess the specific role played by pPv, we considered two simulations without

pPv (A, B) and four with pPv (C-F). The phase transition to pPv is defined with a reference temperature of 2700 K at 2700 km depth. Lateral deviations in the transition depth were determined using the phase function approach of Christensen and Yuen (1985), with a Clapeyron slope that varies from 8 to 16 MPa K^{-1} among the six simulations. The stability field of pPv was further controlled by the temperature at the CMB, T_{cmb}, which is set to 3750 K, on the basis of numerical simulations (Li et al., 2015). As a consequence, one case only displays one phase transition

from bridgmanite (Bm) to pPv (C) while the three others (D-F) present a double crossing i.e. with a second phase change from pPv to Bm located close to the CMB. Finally, the activation energy parameter E_a (see Deschamps et al., 2018) that describes viscosity variations with temperature is lower in two simulations (B, D) when compared to the others (A, C, E, F). This enables us to consider cases with weaker thermochemical piles involving a stronger topography and a smaller area at the CMB. As described below, all other parameters are identical for the six simulations.

These simulations were obtained by solving the conservation of mass, momentum, energy, and composition in a 3D-spherical shell for a compressible, anelastic fluid with infinite Prandtl number. Spherical geometry was modeled using Yin-Yang strips of $128 \times 384 \times 2$ azimuthal cells (corresponding to 512×256 longitude and latitude grid points) with 128 and 64 radial grid points for the cases with and without pPv, respectively, and radial grid refinement at the top and the bottom of the shell. As a result, the bottom 200 km of our models are well sampled by 16 points for the pPv cases, and 8 points for the pPv-free cases. The inner-to-outer radii ratio was fixed to its Earth's mantle value, i.e. 0.55. The compositional field was modeled with a collection of tracers of two types, corresponding to regular (pyrolitic) mantle material and dense material modeling the thermochemical piles (TCPs), possibly corresponding to large low shear velocity provinces (LLSVPs). The compositional field was then inferred from the concentration C of particles of denser material in each cell, which varies between 0 for a cell filled with regular material only, and 1 for a cell filled with denser material only. Note that the exact nature of the compositional field was not prescribed a priori (except for its density excess) in the simulation. Prescribing this nature only matters for the calculation of seismic velocity anomalies, and can be done during post-processing (Section 2.2). The dense material was initially distributed in a basal layer representing 3.5% of the total volume of the shell. The density contrast $\Delta\rho_C$ between the dense and regular materials is controlled by the buoyancy ratio, measuring the ratio between $\Delta\rho_C$ and the density contrast associated with super-adiabatic temperature jump. In all the simulations, this parameter was fixed to 0.23, corresponding to $\Delta\rho_C = 140$ kg m^{-3}. Viscosity was allowed to vary with depth, temperature and composition. In particular, dense mantle material is assumed to be more viscous than regular material by a factor 30, accounting for the fact that it may be enriched in Bm (see Deschamps et al., 2018, for a discussion on this aspect). The potential top-to-bottom thermal viscosity ratio was set to 10^9 or 10^6 for models with $E_a = 20.7$ (A, C, E, F) and $E_a = 13.8$ (B, D), respectively. Due to adiabatic increase of temperature and to the prescription of a temperature offset, the effective viscosity ratio is smaller by about two orders of magnitude. In addition, a viscosity ratio of 30 was added at the limit between the lower and upper mantle, at 660 km-depth, and yield stress was imposed at the top of the shell to avoid the formation of a stagnant lid close to the surface. As a result, the surface horizontal velocity is around 1 cm/year. In addition to the phase change from Bm to pPv mentioned above, the 660-km transition from ringwoodite to Bm was modeled with a discontinuous phase boundary controlled by the definition of a temperature-vs-depth anchor point (here, z = 660 km and T = 1900 km) and a Clapeyron slope (here fixed to −2.5 MPa/K). For additional details on the numerical methods and on the input properties of the simulations, we refer to Tackley (2008) and Deschamps et al. (2018).

With these properties, the system evolves to thermochemical structures that depend at first order on the activation energy E_a. For a stronger (i.e. more viscous) lower mantle ($E_a = 20.7$, cases A, C, E, F), the global pattern consists in one or two large and stable reservoirs of dense material that are also hotter than the surroundings. The distributions of both thermal and compositional anomalies are dominated by very long wavelengths, i.e., spherical harmonic degrees ℓ=2–3. For a weaker lower mantle (E_a=13.8, cases B and D), smaller piles are distributed more homogeneously above the CMB (Fig. 1) with typical

wavelengths corresponding to ℓ=5–10. In both cases, plumes are generated at the top of these reservoirs. pPv is only stable outside these reservoirs. In the representative snapshots we used, the horizontally averaged top and bottom heat flux are about 35–60 and 55–130 mW/m^2, respectively, while the volume average temperature (rescaled with the super-adiabatic temperature jump, here fixed to 2500 K) varies between 1400 and 2100 K (see Table 1). In the bottom 50 km of the shell, the average temperature reaches 3500 K, and the root mean square (rms) lateral temperature anomalies is typically 200 K.

2.2. Computation of seismic velocity anomalies

To calculate shear-wave velocity (V^s) anomalies associated with thermochemical structures obtained by different simulations, we used the method developed in Deschamps et al. (2012), which involves seismic sensitivities, i.e. partial derivatives of seismic velocities to temperature and to various compositional and phase parameters. For each model, temperature anomalies are calculated with respect to the radial profile of horizontally averaged temperature. Because the nature of regular ($C = 0$) and dense ($C = 1$) material in the thermochemical simulation is not a priori prescribed, it should be specified during the calculation of seismic velocity. We assumed that the regular composition is pyrolitic and that dense material is enriched (compared to pyrolitic composition) in iron oxide by 3%, and in Bm by 18%, as suggested by probabilistic tomography (Trampert et al., 2004). Following this assumption, and accounting for the effect of pPv, the V^s-anomalies ($d\ln V^s$) are given by

$$d\ln V^s = \frac{\partial \ln V^s}{\partial T} dT + \frac{\partial \ln V^s}{\partial X_{Fe}} dX_{Fe} + \frac{\partial \ln V^s}{\partial X_{Bm}} dX_{Bm} + \frac{\partial \ln V^s}{\partial X_{pPv}} dX_{pPv} \quad (1)$$

where dT, dX_{Fe}, dX_{Bm}, and dX_{pPv} are local anomalies in temperature, iron, Bm, and pPv. Practically, dT and dX_{pPv} are directly taken from the distributions predicted by the simulation (after rescaling in the case of dT), and dX_{Fe} and dX_{Bm} are deduced from the compositional field following $dX_{Fe} = CdX_{Fe,prim}$ and $dX_{Bm} = CdX_{Bm,prim}$ where $dX_{Fe,prim} = 0.03$ and $dX_{Bm,prim} = 0.18$. Sensitivities of V^s to temperature, iron, and Bm are taken from Deschamps et al. (2012) and account for the presence of pPv (orange curves and shaded areas in their Fig. 6), and were calculated from appropriate equation of state modelling and self-consistent mineralogical dataset. The sensitivity to pPv is based on the compilation of Cobden et al. (2015), which includes a more complete data set for this phase, and is fixed to 2.0×10^{-2}.

2.3. Inferring CMB heat flux from seismic velocity anomalies

Our ultimate goal is to apply insights from the mantle convection simulations (cf. 2.1) to seismic velocity anomalies from lowermost mantle tomography models in order to infer the CMB heat flux pattern. First, the heat flux on the inner boundary of the mantle convection models is calculated based on the temperature distribution at the bottom part of the shell. More specifically, in non-dimensional form, it is written

$$Q_{cmb} = k_{cmb} \frac{(r'^2 - 1)\theta_{cmb} + \theta_1 - r'^2\theta_2}{z_1(1 - r')} \quad (2)$$

where θ_{cmb} and k_{cmb} are the temperature and thermal conductivity at the CMB, θ_1 and θ_2 are the temperatures on the two lowermost grid-points above the CMB (i.e at altitudes z_1 and z_2) and $r' = z_1/z_2$. The use of three grid points enables to better capture the curvature of the temperature profile in this thermal boundary layer. Second, the synthetic seismic velocity anomalies (i.e. based on mantle simulations) are estimated based on the equation of state and assumed appropriate sensitivities (see 2.2). An analytical formalism is derived based on curves of inner boundary heat flux vs. modeled seismic velocity anomalies similar to Nakagawa and Tackley (2008).
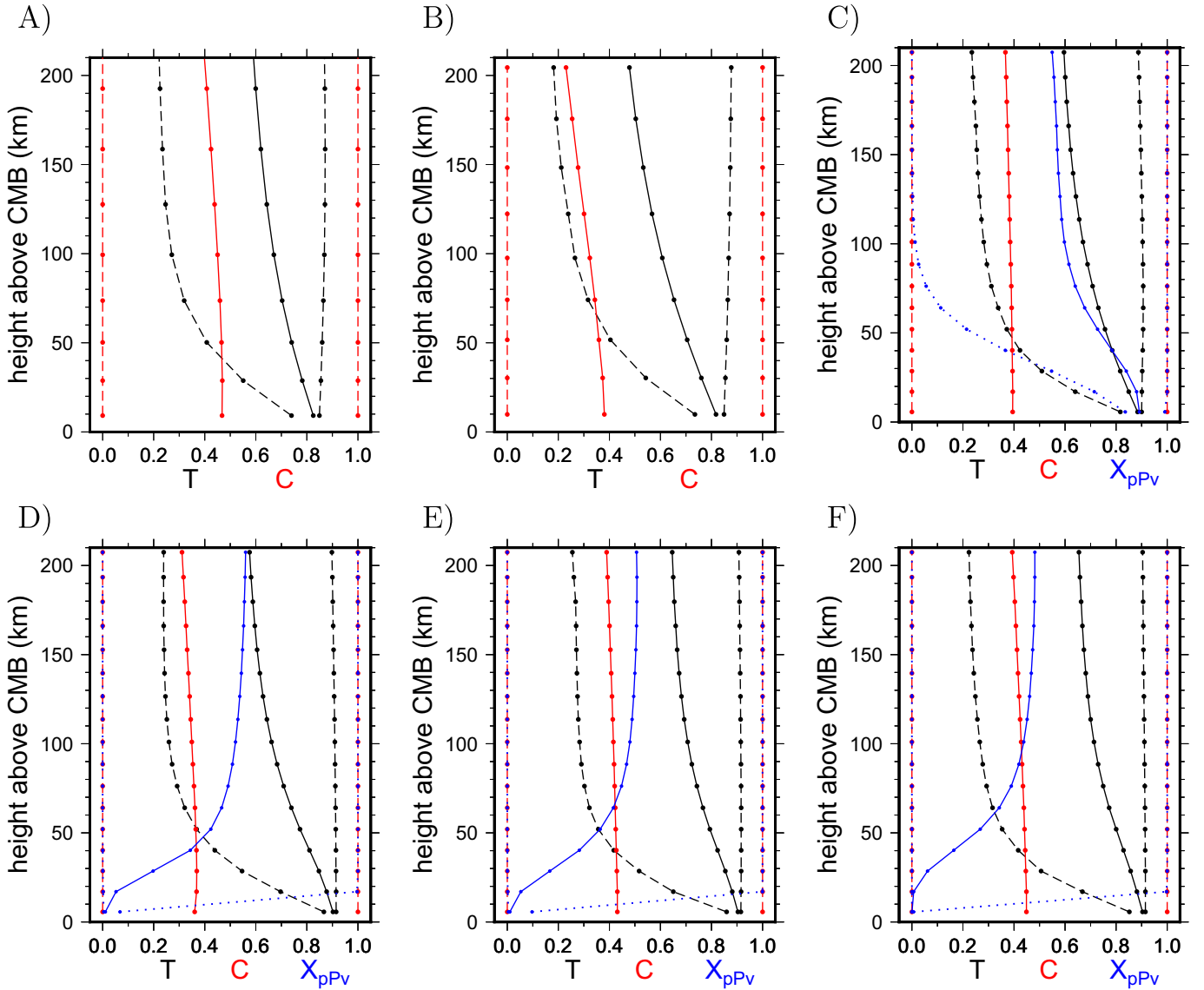
Fig. 2. Radial profiles of dimensionless temperature (black), composition (red) and, when pertinent, pPv fraction (blue) above the CMB for the six simulations (A to F). The solid lines refer to horizontal averages at a given height above the CMB while dashed lines (dotted for X_{pPv}) denote the minimum and maximum values.

Special attention is given to the vertical sampling of the various quantities. The CMB heat flux anomalies q_{cmb} are determined by the temperature right above the CMB. Therefore, only a few radial grid points above the inner boundary, corresponding to a thin thermal layer, are used to calculate the inner boundary heat flux. In contrast, mantle tomography models are obtained from vertically integrated arrival time data. Accordingly, the modeled seismic velocity anomalies $d\ln V_{200}^s$ are calculated from integration over a 200-km thick radial layer.

3. Results

3.1. Variations of temperature, composition and pPv in the 200 km-thick layer above the CMB

The radial parameterization of global tomography models differ from one model to another but typically involves a 100–200 km thick layer above the CMB (cf. e.g. Lekic et al., 2012). We thus consider the 200-km thick bottom part of the spherical shell in numerical simulations of thermochemical convection involving or not a phase change to pPv. All three scalar fields involved in the numerical models (i.e. temperature, composition and pPv) display a specific behavior in this region

(Fig. 2).

Temperature *T* (black curves in Fig. 2). The neighborhood of the CMB is the locus of the hot thermal boundary layer with a typical temperature increase with depth involving several hundreds of K; note that this increase is mostly caused by the increase of temperature in the coldest regions, while the maximal temperature profiles representative of the temperature in the dense, hot thermochemical piles remain approximately constant over this height range above the CMB.

Composition *C* (red curves in Fig. 2). In contrast, this region does not present in our simulations a strong radial gradient of composition owing to the specific nature of thermochemical piles (Tackley, 2012). In this example, piles are stable, thicker than 200 km and do not involve strong topographic variations such as troughs or depressions in this region: this is an outcome of two main controlling parameters, the density and viscosity contrasts associated with the dense layer (Li et al., 2014). As a result, the region with an enriched value of *C* displays sharp steep sides (cf. Fig. 1), a feature that may be shared in the deep mantle by LLSVPs (cf. e.g. Ni et al., 2002).

Fraction of pPv X_{pPv} (blue curves in Fig. 2 C-F). The transition from Bm to pPv occurs above the region of interest: between 380 km (case C) and 470 km above the CMB (case D). As mentioned above, among the
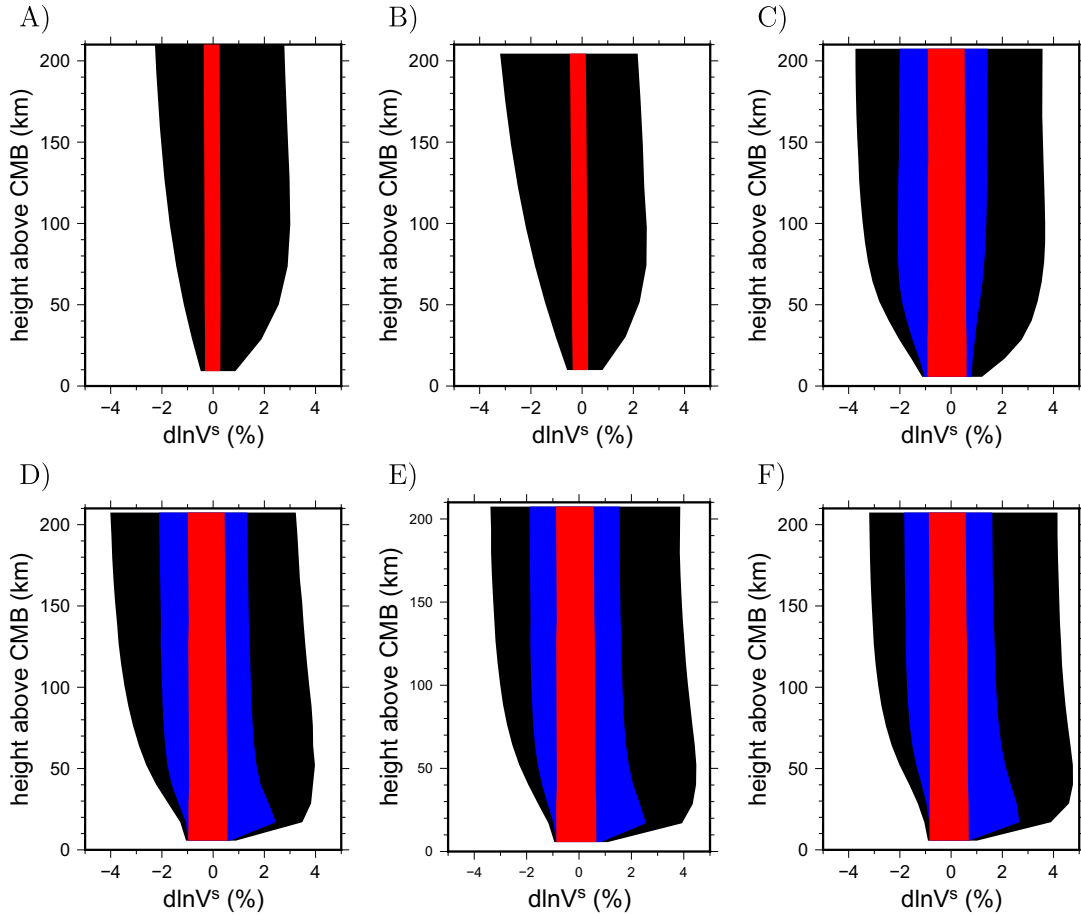
Fig. 3. Contributions of temperature (black), composition (red) and, when pertinent, pPv (blue) to the seismic shear velocity anomalies ($d\ln V^s$) in the 200 km-thick region above the CMB. Cumulative ranges are displayed at each height so that the black contours denote the total anomaly.
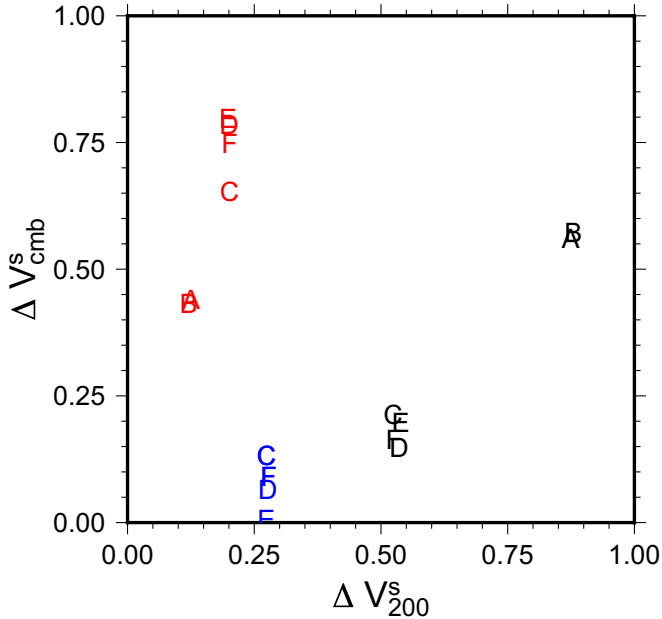

Fig. 4. Relative contributions ΔV^s_{cmb} of temperature (black), composition (red) and, when pertinent, pPv (blue) to ($d\ln V^s$) at the first grid point above the CMB (i.e. 9.2 km for cases A and B, 5.6 km for cases C-F), as a function of the average contribution in the the 200 km-thick region above ΔV^s_{200}. Cases are denoted by the associated letter.

four simulations involving pPv, only one (C) displays a single crossing from Bm to pPv: as a result, in this case, the maximum value of X_{pPv} remains equal to 1 in the 200 km-thick region above the CMB, while the minimum and average values of X_{pPv} increase with decreasing height in the bottom 100-km of the mantle. In contrast, the three other simulations display a double crossing (Hernlund et al., 2005), with pPv transitioning back to Bm in the bottom 100-km. In cases D, E and F, pPv is not present on the CMB but occupies a non-negligible area fraction of the sphere starting from the second grid-point above the CMB. In all four simulations, the area fraction reaches values of 40%-60% at about 100 km above the CMB. The two differing behaviors relate to the choice of the Clapeyron slope and a relatively large temperature at the CMB.

3.2. Contributions to seismic shear velocity anomalies

Fig. 3 displays the contributions of the different fields to the seismic shear velocity anomalies. The relative contributions vary with radius owing to the respective profiles of the three fields (T and X_{pPv} - if applicable - exhibit large radial gradients whereas C does not): the thermal effect (black) gets larger as the distance from the CMB increases while the compositional effect (red) remains similar in amplitude over the whole depth range. It is larger by construction in the cases involving pPv (C-F). The contribution of pPv to the shear velocity anomalies (blue) increases with height above the CMB, up to approximately 100 km: as shown in Fig. 2 C–F, this is caused by an increasing area fraction where pPv is present.

In addition to amplitude effects, a key feature for inferring the CMB's thermal state from tomographic models is the pattern of lateral variations for all fields (including non-thermal) contributing to the seismic
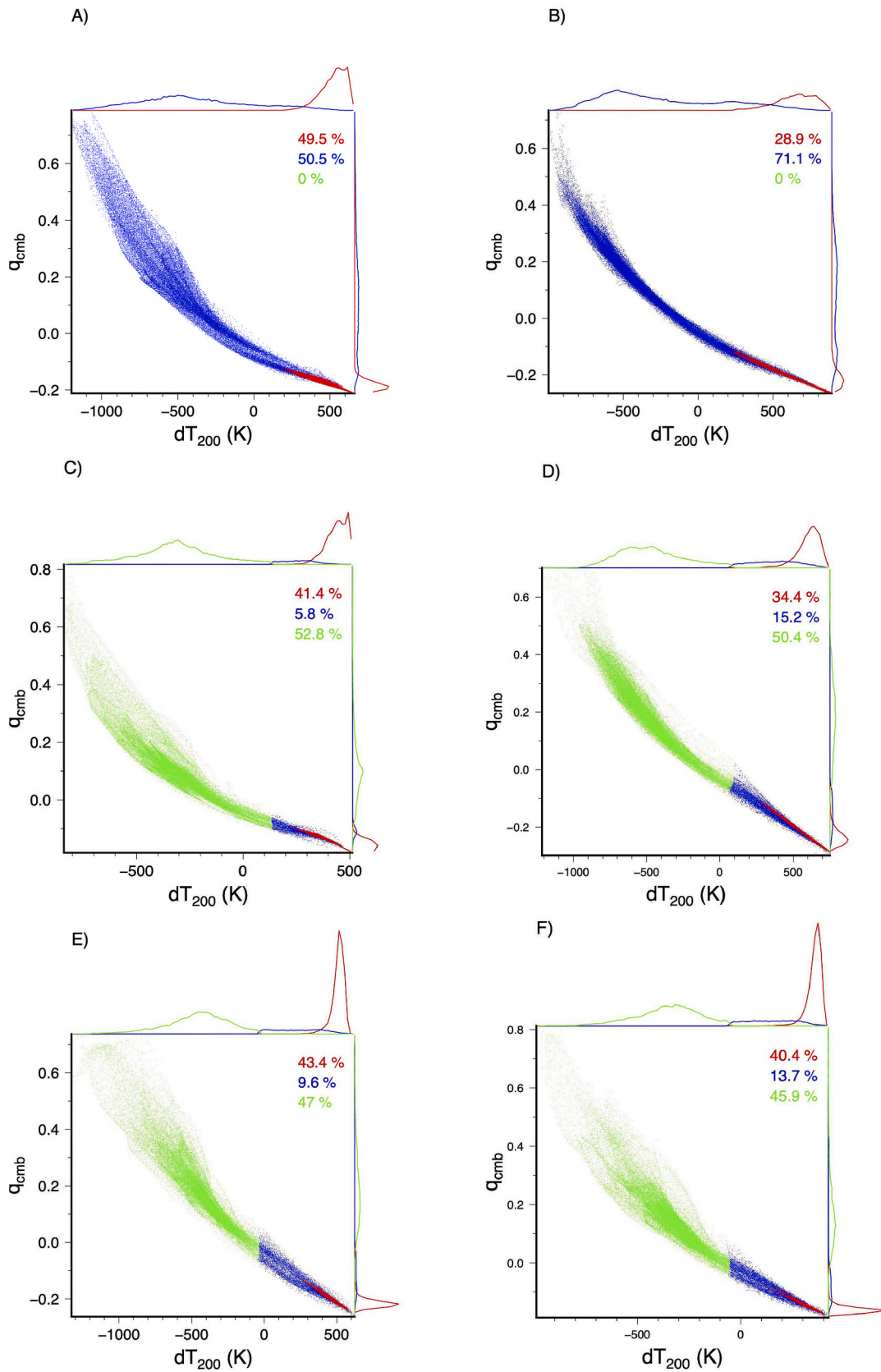
Fig. 5. Relationship between the normalized CMB heat flux anomalies q_{cmb} and the temperature anomalies averaged in a 200 km-thick bottom layer dT_{200} (the latter in K). Each individual dot corresponds to a single doublet of latitude and longitude. Colors indicate the three mantle components: TCPs (red), NM (blue) and pPv (green) with each volumetric fraction given in the legends. Distributions of the probability density for each mantle component are added on top and on the right of each panel, with the same scale.
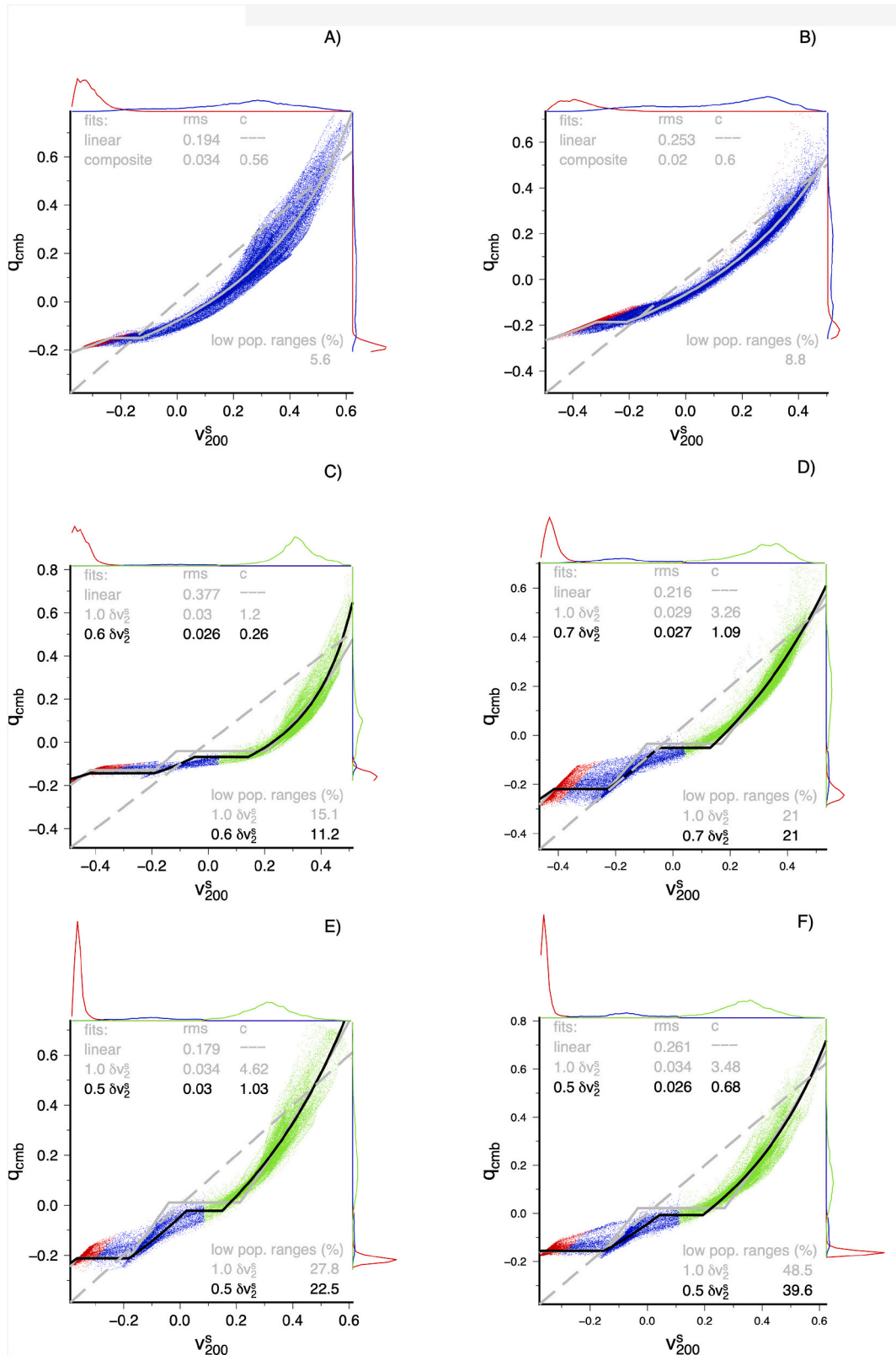
Fig. 6. Relationship between the normalized CMB heat flux q_{cmb} and the normalized seismic shear velocity v_{200}^s. The linear fit is displayed as a dashed grey curve. The fits we propose are shown (solid grey and black curves) with the associated slopes of the fitting function (c values, see Eq. (A.24) in A). In grey, the fit corresponds to a jump δv_2^s that is equal to the total effect of the pPv transition, while in black the size of the jump is only a fraction of the latter (the optimal fraction is indicated). The rms values for the proposed and linear misfits are also displayed as well as the sum of the two populations in the "jumps" zones.

velocities. Fig. 1 precisely displays these patterns for the temperature, the composition and the phase (pPv fraction) fields. The observed features are encouraging in regard to our goal to infer the thermal state immediately above the CMB (q_{cmb}) from the interpretation of $d\ln V^s$ derived from global tomography models (an averaged quantity over 100–200 km). The two challenges mentioned earlier might not represent definite obstacles: (1) in addition to temperature, composition and mineralogy also contribute to the tomographic pattern, but the three fields exhibit a high level of spatial correlation; (2) while large radial temperature and mineralogy gradients exist in this region (so that a radial average could in principle blur the tomographic pattern), the patterns of lateral variations of these fields are similar over the whole depth range. As a result, the existence of a possible surjection between q_{cmb} and $d\ln V^s_{200}$ remains viable.

Significant distortions between the various contributions to the seismic anomalies just above the CMB vs. over a layer of 200 km above it can nevertheless be anticipated as the sensitivity of seismic velocities to the temperature, composition and phase fields vary in this depth range and, more importantly, because the relative contributions of each field vary in this region. This is exemplified in Fig. 4 where the relative contributions of the various fields to V^s is compared between the layer immediately adjacent the CMB (ΔV^s_{cmb}) and in a 200 km-thick layer above it (ΔV^s_{200}), representative of tomography sensing. We emphasize that V^s_{cmb} is not accessed by tomographic models and that it involves a largely arbitrary nature as based on one discrete layer at a distance from the CMB that vary among the simulations, depending on the radial discretization. In addition, while V^s_{cmb} anomalies depend on three fields (temperature, composition, mineralogy), the CMB heat flux anomalies q_{cmb} only depend on the radial temperature gradient. Examining local contributions to V^s above the CMB is nevertheless instructive. In the cases without pPv (A, B), temperature (in black) is the main contributor to V^s anomalies, more than composition, but this predominance is less pronounced (less than 60%) locally above the CMB than in the 200 km-thick average (more than 85%). Such a distortion is also observed for simulations including pPv (C-F) where the contribution of composition (in red) is predominant at the CMB while the contribution of temperature (in black) prevails in the average. As expected, pPv contributes marginally at most in the layer immediately above the CMB where the anomalies in pPv fraction vanish (almost only pPv in the case with a single crossing, C, almost no pPv in cases with a double crossing, D-F), while on average it contributes to more than 25% of the V^s anomalies in the 200 km-thick layer.

The next sections describe in detail the nature of such distortions and how a map of CMB heat flux can in principle be built from seismic velocity anomalies.

3.3. CMB heat flux (local) and temperature (radially averaged)

We have not yet precisely introduced the variable measuring the CMB heat flux anomalies. Our goal is to relate the pattern of heat flux anomalies to a pattern of seismic anomalies and we leave the (important) question of the amplitude of these quantities out of the scope of the present work. We therefore introduce normalized quantities for both, q_{cmb} and v^s_{200}, such that the average of each over the spherical surface is 0 and the range (maximum value minus minimum value) is 1 (cf. A).

For the six simulations, Fig. 5 displays at each location of the discrete mesh on the sphere, the relationship between q_{cmb} and the temperature anomalies (in K) averaged in the 200 km-thick bottom layer (dT_{200}). The ensemble of locations is partitioned in two or three populations representative of the mantle components (depending on whether pPv is present or not): the hot thermochemical piles (in red), which we will note "TCPs" in the following, defined by the criterion $C > 0.5$; the coldest region where pPv is present (in green, when introduced in the simulation), which we will note "pPv", defined by the criterion $X_{pPv} > 0.5$; the normal mantle (in blue), which we will note "NM",

corresponding to the remaining regions.

As expected, the three populations occupy very distinct areas in Fig. 5: TCPs are largely focused at high temperatures and low CMB heat fluxes, while NM and pPv are more diffused toward the colder and higher heat flux regions. In the cases with stronger piles (A, C, E, F, about 40–50%), TCPs represent a larger volume and heat flux variability at low temperatures is larger. In cases with weaker piles, TCPs represent a smaller volume (B, D, about 30–35%), and the heat flux range associated to a given temperature is less spread. TCPs are extremely homogeneous in the simulations presented here (also see Fig. 1) although temperature variations in TCPs tend to be slightly larger in cases where pPv is not introduced (A, B). When pPv is introduced, the pPv component represents the vast majority of the non-TCPs material.

The global shape is quite coherent, for any mantle component, with an expected decrease of q_{cmb} with increasing dT_{200}. The curved shape is related to the shape of the temperature profiles (i.e. almost isothermal for the hottest regions, and with an error function decrease with increasing height for the colder regions, Fig. 2). This was already identified by Nakagawa and Tackley (2008) (see their Fig. 3 for S-wave velocity, corresponding to our Fig. 6). We emphasize that while Nakagawa and Tackley (2008) considered synthetic shear seismic wave anomalies, and thus temperature, at a given depth (2750 km) above the CMB, we opted for an average of the 200 km-thick layer above the CMB, possibly reflecting better the construction of tomographic models. As a result, the curved shape is more pronounced in our results than in theirs. It also involves a different fitting expression and procedure (A).

3.4. CMB heat flux (local) and seismic shear velocities (radially averaged)

Fig. 6 displays the relationship between q_{cmb} and v^s_{200}. The latent heat and geometrical effects (vertical averaging of the temperature field) discussed above for the relationship between q_{cmb} and dT_{200} (Section 3.3) are naturally present. However the probability density distributions for v^s_{200} are spread out on a larger range. As already shown in Fig. 3, systematic shifts in $d\ln V^s_{200}$ are indeed caused by composition (the hottest regions or TCPs, red, are even slower, owing to their enrichment in iron, $d\ln V^s_{200}{}^C = 1.2\%$ for cases where pPv is present, C-F, compared to $d\ln V^s_{200}{}^C = 0.6\%$ when it is not present, A and B) and the presence of pPv (the coldest regions, green, are even faster, $d\ln V^s_{200}{}^{pPv} = 1.6\%$, C-F). Nevertheless, as non-thermal effects are highly correlated spatially with temperature (dense regions are hot, pPv regions, when present, are cold), the overall shape of the v^s_{200}-q_{cmb} mapping is similar to the one between dT_{200} and q_{cmb} (Fig. 5). The three populations are therefore more distinct.

3.5. Mapping CMB heat flux from radially averaged seismic anomalies

We now try to relate explicitly the local normalized heat flux anomalies, q_{cmb}, to the normalized radially-averaged seismic shear velocity anomalies, v^s_{200}. Our procedure first considers a map of seismic velocity anomalies $d\ln V^s_{200}$ and identifies three contributions of temperature (T), composition (C) and mineralogy (pPv)

$$d\ln V^s_{200} = d\ln V^s_{200}{}^T + d\ln V^s_{200}{}^C + d\ln V^s_{200}{}^{pPv} \tag{3}$$

(the second and third terms on the right hand side of Eq. (1), associated to iron content and Bm content, are grouped here in parameter C).

As the three mantle components (TCPs, NM, pPv) are clearly distinct, the last two contributions in Eq. (3) are simple: in an idealized version of the pattern observed in the six simulations (see details in A, Table A.2), $d\ln V^s_{200}{}^C$ is equal to some negative contribution (normalized value δv^s_1) of iron enrichment for TCPs and zero elsewhere (NM, pPv), while $d\ln V^s_{200}{}^{pPv}$ is equal to some positive contribution (normalized value δv^s_2) for pPv and zero elsewhere (TCPs, NM). $d\ln V^s_{200}{}^T$ applies gradually to the
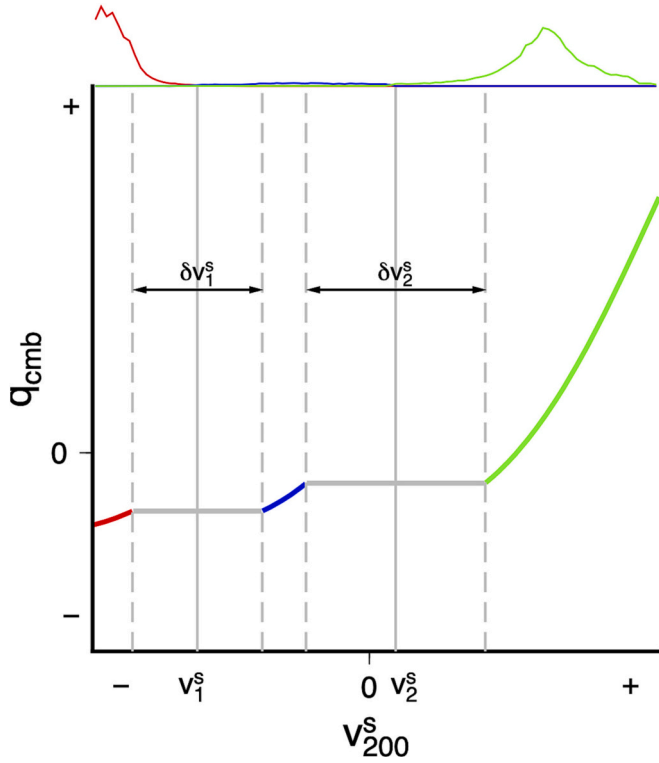
Fig. 7. Principle of the fit proposed for the q_{cmb}-v_{200}^s mapping (cf. Fig. 6 and A). A unique fitting function is introduced for the thermal effect in each of the three mantle components (red: TCPs, blue: NM, green:pPv) with two jumps in-between components (grey). The amplitudes ($\delta v_\bullet^s$) and centers ($v_\bullet^s$) of jumps are also introduced, in relation to the probability density function for the three mantle components, displayed in the panel above, see text for details.
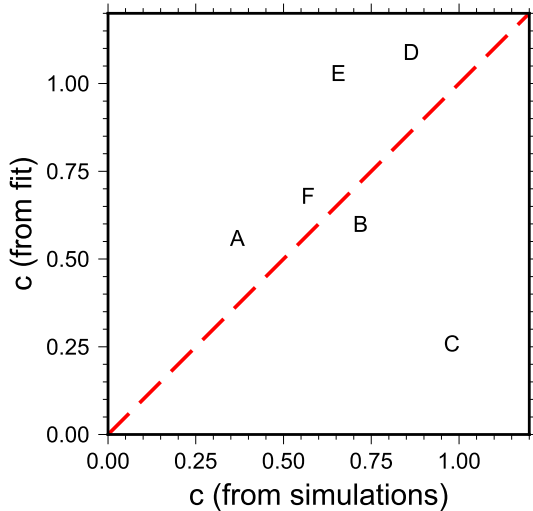

Fig. 8. Fitting parameter c: comparison with heat flux statistics. The y-axis refers to the optimal value of c obtained in the fitting procedure (when pPv is present, we allowed for an additional fitting parameter, the variable jump δv_2^s). The x-axis corresponds to an estimate directly obtained from simulations. The dashed red line indicates $y = x$.

three mantle components from the hot (and slow) TCPs to the cold (and fast) pPv. Assuming this thermal effect is identical for all three mantle components, we propose to fit the observed relationship between q_{cmb} and v_{200}^s by a simple composite function (cf. Fig. 7, also see A): a single function for the thermal effect and two distinct jumps for composition

and mineralogy. In the idealized scheme considered here, the two jumps (only one if pPv is omitted) correspond to empty populations for v_{200}^s. They embody two characteristics of the boundaries between mantle components. First, these boundaries are infinitely sharp and C and X_{pPv} only assume values equal to 0 or 1. In the case of pPv, when considering vertical averaging, this last statement does not hold. While the pattern of pPv averaged over the 200-km thick region is roughly similar to the one at the CMB, we see in Figs. 1 and 2 that the average value evolves radially (mostly in the 100-km layer above the CMB), and anticipate that the effective amplitude of δv_2^s shall represent only a fraction of the full effect corresponding to the difference between no pPv and pure pPv. Second, these boundaries are associated to a single temperature value (i. e. there exist temperatures T_1 and T_2 such that $T < T_2$ in the pPv component, $T_2 < T < T_1$ in the NM component and $T_1 < T$ in the TCP component). In practice, these characteristics are not strictly true and "jumps zones" might correspond to a non negligible fraction of the surface area (see values reported in Fig. 6 as well as pdfs above panels): 10% or smaller for cases A-C, but up to 40%-50% for case F. The latter obviously results from the fact that the jump δv_1^s, related to the effect of composition, involves in practice a major fraction of thermochemical piles. Furthermore, we anticipate that in the case of mantle tomography, regularization aspects might alter the validity of these two conditions (see Section 4).

The proposed relationship for the fit is practically based on a single parameter described below and in A. Even better agreements would naturally be reached if additional fitting parameters were introduced to account for the specific dynamics of the lowermost mantle in each simulation. However, as these lack appropriate constraints when solely a distribution of shear seismic velocity anomalies is considered, such additional parameters would not be tractable.

The obtained best fits always lead to a significant improvement when compared to a linear fit (the latter assuming that q_{cmb} is equal to v_{200}^s, i.e. a purely thermal origin for seismic shear velocities). Typically, the misfit, reported in Fig. 6, is one order of magnitude smaller. More precisely, as expected, the proposed fit ensures to generally capture the curvature of the q_{cmb}-v_{200}^s relationship towards higher flux for positive values of seismic velocity anomaly and conversely, relatively lower flux at lower values.

In the four cases involving the presence of pPv (C-F), we allowed for a variable amplitude of seismic velocity jump δv_2^s that measures the effect of X_{pPv} (black solid curve in Fig. 6, the grey curve corresponds to the full effect). A better fit is of course retrieved for the variable amplitude of δv_2^s, although marginally in terms of rms values for misfit: this is essentially due to the fact that the region adjacent to the boundary between the normal mantle (blue) and pPv (green) englobes a small fraction of the surface area. The latter is witnessed in the value for the "jumps zones" population already discussed, corresponding to jumps δv_1^s and δv_2^s. Decreasing significantly the size of δv_2^s, e.g. halving in cases E and F, only has a moderate effect on the "jumps zones" population, e.g. minus one fifth. Again this is because jump δv_1^s involves a significant fraction of TCPs that are particularly homogeneous and thus correspond to a strong peak in the pdf. The optimal fraction of the full effect, measured by δv_2^s is shown to correlate to the average amount of pPv in the region of interest (see Fig. 2): larger than 0.55 for cases C and D while it is around 0.5 for cases E and F.

As shown in A, parameter c only relates to the absolute heterogeneity in CMB heat flux: $c = \min(Q_{cmb})/(\max(Q_{cmb}) - \min(Q_{cmb}))$. In Fig. 6, we present optimal values for this parameter corresponding to the best fits. These can be compared to the actual statistics of CMB heat flux heterogeneity from the simulations (Fig. 8). Rather than $\min(Q_{cmb})/(\max(Q_{cmb}) - \min(Q_{cmb}))$, we use $(F_b - 0.5\sigma_{F_b})/\sigma_{F_b}$, more representative of the global distribution, e.g. in some simulations $\min(Q_{cmb})$ is negative, in contrast with the simple analysis developed in A, while the latter seems reasonable for the whole distribution. Indeed, the agreement is good for all cases but C, i.e. when pPv is present at the
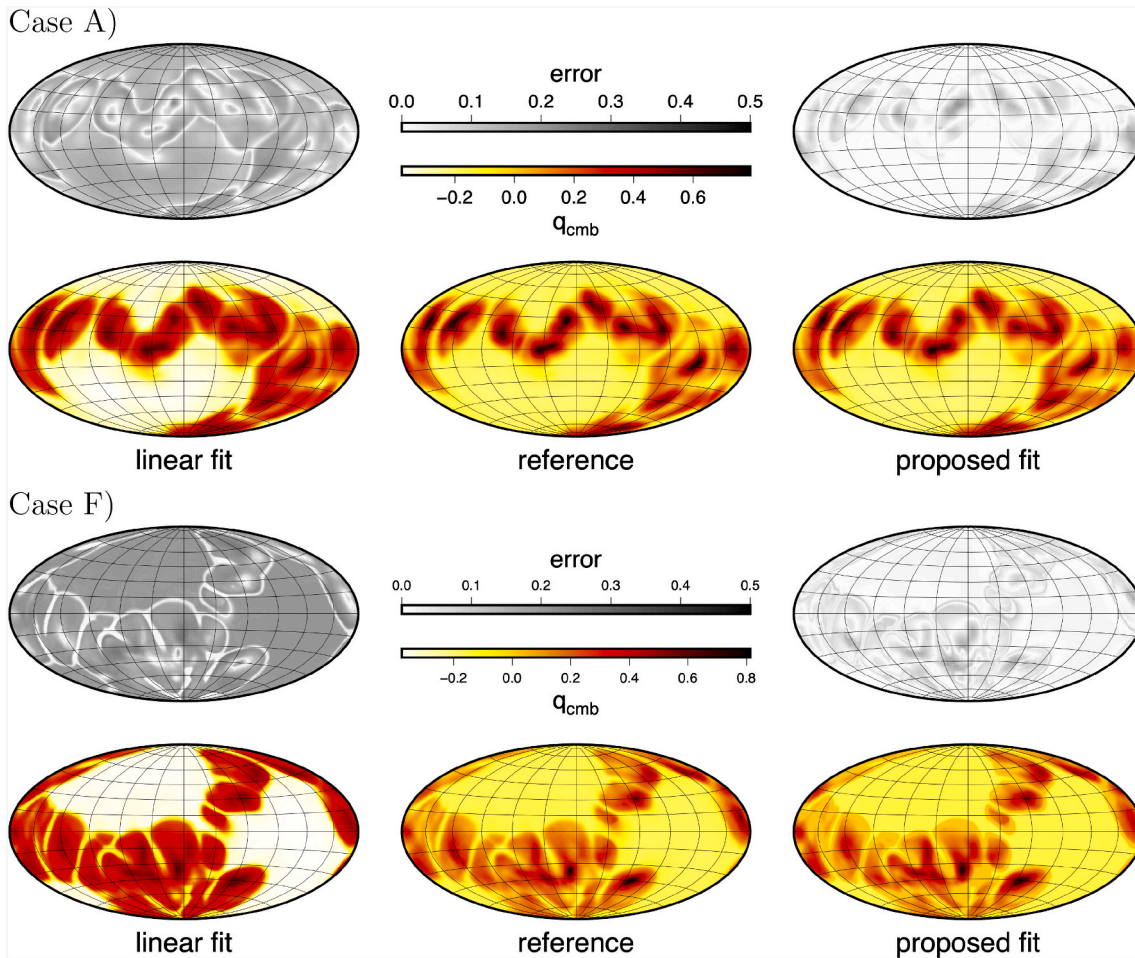
Fig. 9. Comparison of the linear fit (left) and the proposed fit (right) for cases A and F. Bottom row: heat flux q_{cmb}. Top row: error on q_{cmb} (i.e. absolute value of the difference between the fit and the reference). The center panel in the bottom row indicates the reference heat flux (from the simulations).

Table A.2
Idealized pattern for the mantle involved in the fitting procedure.

mantle component	C	X_{pPv}	T range
pPv	0	1	$[T_{min}, T_2]$
NM	0	0	$[T_2, T_1]$
TCP	1	0	$[T_1, T_{max}]$

CMB (double crossing of the pPv phase change). In this specific case, the fit obtained with the value from simulations (0.98, not shown in Fig. 6) is associated to an rms misfit of 0.03. We conclude that a variety of parameterizations provide acceptable fits and that values of c in the simulations are typically in the range $[0.3, 1]$ (see Fig. 8). We further note that when the size of δv_2^s is not inverted for but fixed as the full effect prescribed in the simulations (grey lines in Fig. 6-C to F), the associated value of c is extremely large when compared to a physical interpretation of the slope, an effect of distorting the fit because of a too large jump around v_2^s.

For two emblematic examples (A: no pPv, F: pPv with double crossing), Fig. 9 enables to visualize in terms of pattern what is already shown in Fig. 6 in terms of values. The proposed fit reproduces very well the reference heat flux. In particular, two essential features are very well captured: (1) a higher (less negative) heat flux for TCPs than predicted by the linear approximation, and (2) when pPv is introduced (C, F), the largest heat flux regions at the center of the pPv regions (whether a single or a double crossing is involved) which fade away in the case of a linear approximation. As q_{cmb} averages out to zero by definition, this implies that the intermediate heat flux regions of the NM and the high heat flux regions of the pPv regions correspond to relatively lower values than in the linear approximation.

4. Discussion

4.1. Distinct mantle components

The analysis we propose is based on an idealized pattern for the three mantle components: hot thermochemical piles (TCPs), "normal" mantle (NM) and cold regions with postperovskite (pPv). While this partition seems reasonable for pPv (imposed by the phase diagram) and should remain valid for TCPs (if these present boundaries that are indeed as sharp as suggested for example by Ni et al., 2002), the fact that an average is envisioned on a 200 km-thick mantle layer already involves departure from this idealized scheme. This is manifested in our simulations where the "jumps zones" for $d\ln V_{200}^s$ involve in practice a non-negligible fraction of the pdfs (see color curves above each panel in Fig. 6). Nevertheless, the heat flux predicted by the fit in these "jumps zones" approximates well the pattern obtained in the simulations.

In the Earth, the structure of large-scale mantle components, as illuminated by seismic tomography, can certainly differ from those of the specific mantle simulations chosen here. As already noted, in the simulations, the mantle fraction that includes pPv is a direct consequence of the parametrization adopted for the phase change (Clapeyron slope) and the global thermal state of the mantle (e.g. the CMB temperature). At present, global tomography models do not provide

constraints on the area fraction of pPv-rich mantle: while fast clusters above the CMB in vote maps analyzed by Cottaar and Lekic (2016) are readily associated to slab material, the presence of pPv is not discussed. As a consequence, distinctive interpretations of the same tomography model may be equally plausible.

The population termed "TCPs" in the analysis of the simulations possibly differs from the actual LLSVPs. The precise volume of actual LLSVPs is a matter of debate and the volume in our simulations (3.5 %) is in line with usual estimates (from 2 % to 8 % of the entire mantle, Hernlund and Tackley, 2008; Cottaar and Lekic, 2016). In our simulations, the thermochemical piles are also remarkably homogeneous (both thermally and chemically). This feature is attributable to both a relatively low viscosity and our choice to only consider one chemical composition for the dense layer. While the composition of TCPs is not sufficiently resolved by global seismic tomography models, some advocate that it may be heterogeneous (French and Romanowicz, 2014). Given our model assumption that the dense mantle material is of primordial origin, an obvious source of chemical heterogeneity would be the addition of recycled mid-ocean ridge basaltic material (MORB). In their pioneering effort to relate CMB heat flux from mantle convection simulations to shear velocity anomalies, Nakagawa and Tackley (2008) have opted for a purely basaltic interpretation of thermochemical pile material. In terms of seismic velocity, the latter is associated to a faster velocity than normal mantle so that thermochemical piles are not LLSVPs in their model. However, it should be pointed out that the exact influence of MORB on shear velocity depends on the assumed MORB composition in main oxides. Available compositions are rather dispersed, altering *in fine* MORB signatures (Deschamps et al., 2012). A mixture of primordial and recycled material for TCPs is more likely and its pdf could be more complex.

While significant jumps in seismic anomalies might be present in the mantle above the CMB, it is also possible that tomography models blur laterally this signal through damping and smoothing. In this case, even if distinguishing the various mantle components is achieved easily on a 200-km averaged layer extracted from mantle simulations (Fig. 6), the same exercise might not be as simple when applied to the pdf derived from tomography models.

4.2. Jumps in seismic velocities

Individual probability density functions of mantle components in the simulations are used to identify the values $v_\bullet^s$ of boundaries between mantle components. In practice, these are not known a priori, i.e. the spherical distribution of $d\ln V_{200}^s$ is obtained from the lowermost layer of a tomography model, and only the global probability density is available. We note that locations $v_\bullet^s$ could arguably be estimated as local minima in such a pdf, albeit predictably in a much less precise way.

Similarly, in the above analysis, amplitudes of jumps ($\delta v_\bullet^s$) are directly derived from values prescribed in the simulations. In the absence of such a knowledge for the Earth's mantle, these can be estimated from mineral physics. Uncertainties on elastic moduli of lower mantle minerals (and thus on shear velocity sensitivities to temperature, composition and phase) remain large. However, it is important to note that there is a consensus on the trends, i.e., shear waves travel slower in regions with excess iron, and faster in pPv and in regions enriched in Bm.

4.3. Overall applicability of the proposed scheme

Two prerequisites enable the application of the scheme proposed above. First, for dynamical reasons, the three main populations for the deepest mantle considered here (TCPs, normal mantle, pPv) are not too well-mixed. Second, the jumps in seismic anomalies associated to compositional (TCPs to NM) and mineralogical (NM to pPv) changes are sufficiently significant to detect these components in pdfs of shear wave velocity anomalies.

The first condition is obviously valid in our mantle simulations. It is also valid in most dynamical interpretations of seismic velocity anomalies, whether thermochemical piles (e.g. McNamara and Zhong, 2005; Deschamps and Tackley, 2009) are indeed present in the Earth mantle as in the mantle simulations, or if purely thermal plume clusters explain LLSVPs (see e.g. Bull et al., 2009; Davies et al., 2012) as the partition between normal mantle and LLSVPs would then be trivial. One possible complexity is that, because iron-rich Bm transforms to pPv at lower pressure than pure Mg-Bm (see Cobden et al., 2015), patches of pPv may exist at the bottom of LLSVPs, despite the high temperature of these regions. Numerical simulations indicate that transient pPv patches can form at the base of hot piles (Li et al., 2016), and it has further been suggested that the ultra-low velocity zones (ULVZs) observed at the bottom of the mantle (see Yu and Garnero, 2018, for a review) may be small patches of iron-rich pPv (Mao et al., 2006). Basal pPv patches within LLSVPs would however be limited in size, typically a few hundreds of kilometers in length and a few tens in thickness, such that their seismic signal would be diluted in tomographic models hence their impact on the CMB heat flux would be limited.

The second condition further requires knowledge of the composition of the deepest mantle. More specifically, while several hints indicate that LLSVPs are compositionally different from the surrounding mantle (assumed to be pyrolitic), the exact nature of these regions remains debated. Considering that mantle rocks are built from five main oxides (SiO_2, MgO, FeO, Al_2O_3 and CaO), an iron (FeO) excess (compared to pyrolitic value) is often advocated because it is consistent with the observed drop in V^s (Deschamps et al., 2012), and is further supported by the density excess reported by tidal tomography (Lau et al., 2017), normal modes (other than Stoneley modes) (Trampert et al., 2004; Mosca et al., 2012), and 6-year variations in the length-of-the day (Ding and Chao, 2018). In addition to iron excess, TCPs may contain more Bm (Trampert et al., 2004) to explain the anti-correlation between V^s and bulk-sound velocity. These conclusions are supported by a principal component analysis (Vilella et al., 2020), which includes the effects of aluminum, calcium, and oxidation state. Assuming the MORB composition of Workman and Hart (2005), with 49.5% SiO_2, 8.0% FeO, and 9.7 MgO%, and based on numerical simulations of thermo-chemical convection including basalt formation and recycling, Jones et al. (2020) found that the bottom 100–200 km of TCPs could be entirely composed of MORB. By contrast, taking into account the strong dispersion in MORB composition, Deschamps et al. (2012) showed that TCPs entirely composed of recycled MORBs would require very large temperature excess, and thus appear less likely. However, small fractions of MORBs may enter TCPs (Li et al., 2014), as proposed in the heterogeneous basal melange (BAM) scenario (Tackley, 2012).

Alternatively, it has been suggested that LLSVPs may be stratified in a layer of primordial material at the bottom covered by a layer of recycled MORBs (Ballmer et al., 2016). If the the layer or primordial material is thick enough (> 200 km), as suggested by Ballmer et al. (2016), the presence of recycled MORBs above it would not affect our approach. A thinner layer of primordial material may have stronger impact on the calculation of shear-velocity, which may in turn affect parameter values in our fitting function (A), but not the overall approach. Additional simulations may however be needed to infer these parameters.

An effect that may influence CMB heat flux but is not accounted for in our calculations is the change of thermal conductivity with temperature and composition. At lower mantle conditions, thermal conductivity might be controlled by lattice vibrations rather than radiative heat transfer (e.g. Keppler et al., 2008; Kavner and Rainey, 2016). In the past decades mineral physics experiments that measured lattice thermal conductivities of lower mantle minerals up to CMB pressures (Hsieh et al., 2017, 2018; Ohta et al., 2012, 2017) showed that these conductivities decrease with increasing fraction of iron oxide. In addition, mantle minerals conductivities decrease with increasing temperature as $1/T^n$, with n around 0.5 or lower (Klemens et al., 1962; Manthilake

et al., 2011; Dalton et al., 2013). Interestingly, these trends amplify the heat flux changes related to lateral variations in the radial thermal gradient, as the conductivity of cold slabs (hot and iron-rich piles) would be higher (lower) than that of average, pyrolytic mantle. Based on Hsieh et al. (2017, 2018) experimental data and on thermo-chemical distributions deduced from probabilistic tomography (Trampert et al., 2004; Mosca et al., 2012), Deschamps and Hsieh (2019) estimated lateral changes in thermal conductivity in the lowermost mantle and their associated variations in CMB heat flux. These calculations indicate that conductivity changes with temperature and composition may induce heat flux anomalies around $\pm$ 20%, compared to the horizontal average, but the heat flux is still controlled by lateral changes in the thermal gradient. Overall, accounting for lateral variations in thermal conductivity is expected to mostly affect the CMB heat flux amplitude and less its pattern, with the latter being the focus of this study.

5. Conclusions

If the two conditions listed above in Section 4.3 prevail, any tomographic model can in principle be interpreted in terms of CMB heat flux patterns using the procedure we propose with the thermal effect described as a curved function. The latter mimics the relationship between heat flux and local temperature variations immediately above the CMB to temperatures averaged over $\simeq$ 200-km, i.e. the typical radial resolution of global tomography models. Two discrete jumps are supplemented, associated to composition and mineralogy (if pPv-rich regions are present).

A detailed application of this method shall involve various tomographic models and consider various jump values. The main effect of our interpretation relative to a linear relationship between heat flux and seismic velocity appears to be that of an attenuation of negative heat flux regions (i.e. hot mantle such as TCPs) while large heat flux regions (i.e. cold mantle) become more pronounced. Moderate heat flux regions become relatively weaker. A detailed application of this method shall involve sensitivity tests to the chosen tomographic model and the prescribed jump values. The consequences of such a distortion of the inferred CMB heat flux pattern on the geodynamo shall be the topic of future studies.

Declaration of Competing Interest

The authors declare the following financial interests/personal relationships which may be considered as potential competing interests: Choblet reports financial support was provided by Agence Nationale de la Recherche.

Data availability

No data was used for the research described in the article.

Acknowledgments

Appendix A. Mathematical formulation of the composite fit

A.1. Definition of variables

Numerous variables have been introduced for the same physical quantities: specific definitions are listed below.

notation	meaning
CMB heat flux:	
F_b	average flux (mW m^{-2})
Q_{cmb}	dimensionless flux
Q'_{cmb}	dimensionless flux with alternative temperature scale (only in A.3)
q_{cmb}	normalized flux anomaly (with a unity range and zero mean)
q	normalized flux (ranging between 0 and 1)
shear-wave velocity:	
V^s	velocity
$\frac{\partial \ln V^s}{\partial \bullet}$	partial derivative relative to $\bullet$
$d\ln V^s$	velocity anomaly
$d\ln V^s_{200}$	velocity anomaly averaged over the bottom 200-km
$d\ln V^s_{200}{}^T$	temperature contribution to $d\ln V^s_{200}$
v^s_{200}	normalized velocity anomaly (with a unity range and zero mean)
v^s_1, v^s_2	location of velocity jumps (relative to v^s_{200})
$\delta v^s_1, \delta v^s_2$	amplitude of velocity jumps (relative to v^s_{200})
v^T	normalized temperature contribution to velocity (ranging between 0 and 1)
v	normalized velocity (ranging between 0 and 1)
temperature:	
T	temperature (in K)
T_{cmb}	temperature at the CMB (in K)
T_{200}	temperature averaged over the bottom 200-km (in K)
dT	temperature anomaly (in K)
θ	dimensionless temperature
θ'	alternative dimensionless temperature (only in A.3)
θ_{cmb}	dimensionless temperature at the CMB
θ_{200}	normalized value of T_{200} (ranging between 0 and 1)

A.2. Normalized anomalies and seismic velocity jumps

The normalized anomalies for heat flux q_{cmb} (and likewise for seismic anomalies, v_{200}^s) used in the main text, whose average value is 0 on the spherical surface, are simply related to the normalized heat flux q (and seismic velocities v) ranging between 0 and 1,

$$q\left(\vartheta, \phi\right) = \frac{q_{\mathrm{cmb}}(\vartheta, \phi) - \min(q_{\mathrm{cmb}})}{\max(q_{\mathrm{cmb}}) - \min(q_{\mathrm{cmb}})} \tag{A.1}$$

and

$$v\left(\vartheta, \phi\right) = \frac{d\ln V_{200}^s(\vartheta, \phi) - \min\left(d\ln V_{200}^s\right)}{\max\left(d\ln V_{200}^s\right) - \min\left(d\ln V_{200}^s\right)} \tag{A.2}$$

where latitude ϑ and longitude ϕ are introduced at a given location and min and max denote the minimum and maximum value on the sphere. We also introduce the normalized temperature anomalies averaged over the 200-km thick region of interest

$$\theta_{200}\left(\vartheta, \phi\right) = \frac{T_{200}(\vartheta, \phi) - \min(T_{200})}{\max(T_{200}) - \min(T_{200})} \tag{A.3}$$

Conversely, the normalized anomalies are

$$q_{\mathrm{cmb}} = q - \langle q \rangle \tag{A.4}$$

$$v_{200}^s = v - \langle v \rangle \tag{A.5}$$

where $\langle \bullet \rangle$ means average of $\bullet$ over the spherical surface.

A rigorous formulation for the composite fit involves the introduction of an additional intermediate variable, namely the normalized thermal component of the seismic velocity anomaly (v^T) that ranges between 0 and 1:

$$v^T\left(\vartheta, \phi\right) = \frac{d\ln V_{200}^s{}^T(\vartheta, \phi) - \min\left(d\ln V_{200}^s{}^T\right)}{\max\left(d\ln V_{200}^s{}^T\right) - \min\left(d\ln V_{200}^s{}^T\right)} \tag{A.6}$$

In the simulations, Eq. (A.6) suffices to compute v^T. It is however useful to relate v^T to the normalized seismic velocity v used in the main text

$$\begin{cases} v^T = \dfrac{v - \delta v_1^s - \delta v_2^s}{1 - \delta v_1^s - \delta v_2^s} & \text{if} & v > v_2^s + \dfrac{\delta v_2^s}{2} \\[2mm] v^T = \dfrac{v_2^s - \delta v_1^s - \delta v_2^s/2}{1 - \delta v_1^s - \delta v_2^s} & \text{if} & v_2^s + \dfrac{\delta v_2^s}{2} > v > v_2^s - \dfrac{\delta v_2^s}{2} \\[2mm] v^T = \dfrac{v - \delta v_1^s}{1 - \delta v_1^s - \delta v_2^s} & \text{if} & v_2^s - \dfrac{\delta v_2^s}{2} > v > v_1^s + \dfrac{\delta v_1^s}{2} \\[2mm] v^T = \dfrac{v_1^s - \delta v_1^s/2}{1 - \delta v_1^s - \delta v_2^s} & \text{if} & v_1^s + \dfrac{\delta v_1^s}{2} > v > v_1^s - \dfrac{\delta v_1^s}{2} \\[2mm] v^T = \dfrac{v}{1 - \delta v_1^s - \delta v_2^s} & \text{if} & v_1^s - \dfrac{\delta v_1^s}{2} > v \end{cases} \tag{A.7}$$

where the centers $v_\bullet^s$ of jumps (with $\bullet \in \{1, 2\}$) are dictated by the probability densities of mantle components (v_1^s delimitates v^s values where TCP (lower values) and NM (higher values) are predominant, v_2^s delimitates NM and pPv, and the amplitudes of the jumps $\delta v_\bullet^s$ correspond to the values prescribed numerically:

$$\delta v_1^s = \frac{\delta \ln V_{200}^s{}^C - \min\left(d\ln V_{200}^s\right)}{\max\left(d\ln V_{200}^s\right) - \min\left(d\ln V_{200}^s\right)} \tag{A.8}$$

and

$$\delta v_2^s = \frac{\delta \ln V_{200}^s{}^{pPv} - \min\left(d\ln V_{200}^s\right)}{\max\left(d\ln V_{200}^s\right) - \min\left(d\ln V_{200}^s\right)} \tag{A.9}$$

Such relationships assume a simplified pattern where the composition and mineralogy fields, C and X_{pPv} have only values of 0 or 1 and that the temperature ranges associated to each mantle component constitute a partition of the global temperature range (see Table A.2). Only then is Eq. (A.7) supplemented by Eqs. (A.8) and (A.9) equivalent to Eq. (A.6).

In practice, when averaged over the bottom 100-km of the mantle (see Fig. 2), X_{pPv} ranges between a strictly positive value and 1. We thus allow in the following δv_2^s to be a fraction of the full effect corresponding to X_{pPv} varying between 0 and 1.

A.3. Scaling relationship between CMB heat flux and temperature averaged over a 200-km thick region above the CMB

As proposed by Nakagawa and Tackley (2008), the laterally averaged temperature profile above the CMB can be described by an error function (erf)

$$T\left(R\right) = T_{\text{cmb}} - \Delta T \text{erf}\left[\frac{(R - R_{cmb})\sqrt{\pi} F_b}{2k\Delta T}\right] \tag{A.10}$$

Here, all variables are dimensional and ΔT refers to a local temperature difference between the CMB and that in the well mixed convecting interior. This leads in the dimensionless form

$$\theta'\left(r\right) = 1 - \text{erf}\left[\frac{\sqrt{\pi} Q'_{\text{cmb}}}{2} r\right] \tag{A.11}$$

where $\theta'(r)$ ranges from 1 (at the CMB) to 0 in the well mixed interior of the mantle. Again, Q'_{cmb} is made dimensionless with a local temperature difference.

Integrating $\theta'(r)$ between $r = 0$ and $r = \delta$ (the top of the 200-km thick averaging region for seismic tomography) provides the average temperature in the bottom layer

$$\overline{\theta} = \frac{1}{\delta}\int_0^\delta \theta'\left(r\right) dr = 1 - \frac{1}{\delta}\int_0^\delta \text{erf}\left[\frac{\sqrt{\pi} Q'_{\text{cmb}}}{2} r\right] dr \tag{A.12}$$

With a variable change,

$$\overline{\theta} = 1 - \frac{1}{\alpha\delta}\int_0^{\alpha\delta} \text{erf}[h] dh \tag{A.13}$$

where $\alpha = \frac{\sqrt{\pi} Q'_{\text{cmb}}}{2}$, so that, after integration

$$\overline{\theta} = \theta'(\delta) + \frac{2}{\pi Q'_{\text{cmb}}\delta}\left[1 - \exp\left(-\frac{\pi Q'^2_{\text{cmb}}}{4}\delta^2\right)\right] \tag{A.14}$$

In the regime of interest $\delta \sim .1$ and $Q'_{\text{cmb}} \sim 30$. In this case, $\theta'(\delta)$ and the exponential term are close to 0 and

$$\overline{\theta} \simeq \frac{2}{\pi Q'_{\text{cmb}}\delta} \tag{A.15}$$

A.4. Lateral variations

The above derivations (Eqs. (A.10)–(A.15)) are strictly proposed for a laterally averaged temperature profile. Simulation results show however that significant lateral temperature variations exist (Fig. 2): these are precisely what we want to capture in the mapping as local variations in the temperature gradients above the CMB control q (and q_{cmb}), and lateral variations in temperature in the 200-km thick (or thickness δ) region above the CMB control v (and v^δ_{200}).

In an effort to assess lateral variations of temperature, we remind that the value $\theta'(\delta) = 0$ refers to a local minimum at height δ. Lateral variations of $\overline{\theta}$ would then correspond to

$$\overline{\theta}\left(\vartheta, \phi\right) = \frac{\overline{T}(\vartheta, \phi) - T(\delta, \vartheta, \phi)}{T_{\text{cmb}} - T(\delta, \vartheta, \phi)} \tag{A.16}$$

Similarly, the heat flux should be rescaled to account for lateral variations and we thus introduce

$$Q_{\text{cmb}}\left(\vartheta, \phi\right) = Q'_{\text{cmb}}\left(\vartheta, \phi\right) \frac{T_{\text{cmb}} - T_{\text{surf}}}{T_{\text{cmb}} - T(\delta, \vartheta, \phi)} \tag{A.17}$$

Eq. (A.15) then becomes

$$\overline{\theta}\left(\vartheta, \phi\right) = \theta\left(\delta, \vartheta, \phi\right) + \frac{2}{\pi Q_{\text{cmb}}(\vartheta, \phi)\delta} \tag{A.18}$$

where θ is the dimensionless temperature in the simulations (i.e, the total non-adiabatic temperature difference is used as a characteristic scale).

A.5. Return to normalized anomalies q, θ_{200} and v^T

The normalized quantities introduced above (A.2), θ_{200} and q range between 0 and 1. These are related to $\bar{\theta}$ and Q_{cmb} in the following way

$$\theta_{200}\left(\vartheta, \phi\right) = \frac{\bar{\theta}(\vartheta, \phi) - \min(\bar{\theta})}{\max(\bar{\theta}) - \min(\bar{\theta})} = \frac{\bar{\theta}(\vartheta, \phi) - \min(\bar{\theta})}{\Delta\theta} \tag{A.19}$$

and

$$q\left(\vartheta, \phi\right) = \frac{Q_{cmb}(\vartheta, \phi) - \min(Q_{cmb})}{\max(Q_{cmb}) - \min(Q_{cmb})} = \frac{Q_{cmb}(\vartheta, \phi) - \min(Q_{cmb})}{\Delta Q_{cmb}} \tag{A.20}$$

Eq. (A.18) thus translates into

$$\theta_{200} = \frac{\theta(\delta) - \min(\bar{\theta})}{\Delta\theta} + \frac{2}{\pi\Delta\theta(q\Delta Q_{cmb} + \min(Q_{cmb}))\delta} = a + \frac{b}{q+c} \tag{A.21}$$

Owing to the normalization, the three coefficients a, b and c are related. For instance, $a = -c$. We only use $c = \frac{\min(Q_{cmb})}{\Delta Q_{cmb}}$ that measures the amplitude of heat flux variations at the CMB. It finally comes that

$$\theta_{200} = c\left[\frac{1+c}{q+c} - 1\right] \tag{A.22}$$

Since the normalized thermal component of the seismic velocity anomaly, v^T (also ranging between 0 and 1), is simply equal to $1 - \theta_{200}$, Thus

$$v^T = 1 - c\left[\frac{1+c}{q+c} - 1\right] \tag{A.23}$$

or

$$q = \frac{cv^T}{1 - v^T + c} \tag{A.24}$$

A.6. Proposed algorithm

The algorithm to produce q_{cmb} from the knowledge of the spherical distribution of $d\ln V^s_{200}$ and the centers ($v^s_\bullet$) and amplitudes ($\delta v^s_\bullet$) of jumps, would then be:

1. first compute the normalized seismic velocity v (ranging between 0 and 1, Eq. (A.2)), then its anomaly v^s_{200} (with a zero mean, Eq. (A.5)),
2. compute the normalized temperature contribution v^T (ranging between 0 and 1, Eq. (A.7)),
3. compute the normalized CMB heat flux q (ranging between 0 and 1, Eq. (A.24)), then its anomaly q_{cmb} (with a zero mean, Eq. (A.4)).

Note that step (3) involves the a priori choice of a value for c. We have shown that the latter relates (Eq. (A.18)) to the statistics of q (or, alternatively, if parameter a is chosen, of θ_{200}). Further work would be required to analyse this relationship in more details. In the six simulations presented here, c varies in the range $[0.3, 1]$. The general outcome of the composite fit (a curved function complemented by jumps, Fig. 7) is only moderately affected by the choice of this value (see the various curvatures in Fig. 6).

References

Amit, H., Choblet, G., 2009. Mantle-driven geodynamo features - effects of post-Perovskite phase transition. Earth Planet. Space 61, 1255–1268.

Amit, H., Choblet, G., 2012. Mantle-driven geodynamo features - Effects of compositional and narrow D" anomalies. Phys. Earth Planet. Inter. 190, 34–43.

Amit, H., Choblet, G., Olson, P., Monteux, J., Deschamps, F., Langlais, B., Tobie, G., 2015a. Towards more realistic core-mantle boundary heat flux patterns: a source of diversity in planetary dynamos. Progress Earth Plan. Sci. 2 (1), 1–26.

Amit, H., Deschamps, F., Choblet, G., 2015b. Numerical dynamos with outer boundary heat flux inferred from probabilistic tomography-consequences for latitudinal distribution of magnetic flux. Geophys. J. Int. 203 (2), 840–855.

Aubert, J., Aurnou, J., Wicht, J., 2008. The magnetic structure of convection-driven numerical dynamos. Geophys. J. Int. 172 (3), 945–956.

Ballmer, M.D., Schumacher, L., Lekic, V., Thomas, C., Ito, G., 2016. Compositional layering within the large low shear-wave velocity provinces in the lower mantle. Geochem. Geophys. Geosyst. 17 (12), 5056–5077.

Biggin, A.J., Steinberger, B., Aubert, J., Suttie, N., Holme, R., Torsvik, T.H., van der Meer, D.G., van Hinsbergen, D.J.J., 2012. Possible links between long-term geomagnetic variations and whole-mantle convection processes. Nat. Geosci. 5, 526–533.

Bull, A.L., McNamara, A.K., Ritsema, J., 2009. Synthetic tomography of plume clusters and thermochemical piles. Earth Planet. Sci. Lett. 278, 152–162.

Choblet, G., Amit, H., Husson, L., 2016. Constraining mantle convection models with palaeomagnetic reversals record and numerical dynamos. Geophys. J. Int. 207 (2), 1165–1184.

Christensen, U.R., Aubert, J., 2006. Scaling properties of convection-driven dynamos in rotating spherical shells and application to planetary magnetic fields. Geophys. J. Int. 166, 97–114.

Christensen, U.R., Olson, P.L., 2003. Secular variation in numerical geodynamo models with lateral variations of boundary heat flow. Phys. Earth Planet. Inter. 138, 39–54.

Christensen, U.R., Yuen, D.A., 1985. Layered convection induced by phase transition. J. Geophys. Res. 90, 10291–10300.

Cobden, L., Thomas, C., Trampert, J., 2015. Seismic detection of post-perovskite inside the earth. In: The Earth's heterogeneous mantle. Springer, pp. 391–440.

Cottaar, S., Lekic, V., 2016. Morphology of seismically slow lower-mantle structures. Month. Not. Roy. Astron. Soc. 207 (2), 1122–1136.

Dalton, D.A., Hsieh, W.-P., Hohensee, G.T., Cahill, D.G., Goncharov, A.F., 2013. Effect of mass disorder on the lattice thermal conductivity of mgo periclase under pressure. Sci. Rep. 3 (1), 1–5.

Davies, D.R., Goes, S., Davies, J.H., Schuberth, B.S.A., Bunge, H.-P., Ritsema, J., 2012. Reconciling dynamic and seismic models of Earth's lower mantle: The dominant role of thermal heterogeneity. Earth Planet. Sci. Lett. 353, 253–269.

Deschamps, F., Cobden, L., Tackley, P.J., 2012. The primitive nature of large low shear-wave velocity provinces. Earth Planet. Sci. Lett. 349, 198–208.

Deschamps, F., Hsieh, W.-P., 2019. Lowermost mantle thermal conductivity constrained from experimental data and tomographic models. Geophys. J. Int. 219 (Suppl. 1), S115–S136.

Deschamps, F., Konishi, K., Fuji, N., Cobden, L., 2019. Radial thermo-chemical structure beneath western and northern pacific from seismic waveform inversion. Earth Planet. Sci. Lett. 520, 153–163.

Deschamps, F., Rogister, Y., Tackley, P.J., 2018. Constraints on core–mantle boundary topography from models of thermal and thermochemical convection. Geophys. J. Int. 212 (1), 164–188.

Deschamps, F., Tackley, P.J., 2009. Searching for models of thermo-chemical convection that explain probabilistic tomography. II-Influence of physical and compositional parameters. Phys. Earth Planet. Inter. 176, 1–18.

Ding, H., Chao, B.F., 2018. A 6-year westward rotary motion in the earth: Detection and possible micg coupling mechanism. Earth Planet. Sci. Lett. 495, 50–55.

French, S., Romanowicz, B., 2014. Whole-mantle radially anisotropic shear velocity structure from spectral-element waveform tomography. Geophys. J. Int. 199 (3), 1303–1327.

Glatzmaier, G.A., Coe, R.S., Hongre, L., Roberts, P.H., 1999. The role of the Earth's mantle in controlling the frequency of geomagnetic reversals. Nature 401, 885–890.

Gubbins, D., Sreenivasan, B., Mound, J., Rost, S., 2011. Melting of the Earth's inner core. Nature 473, 361–363.

Gubbins, D., Willis, P., Sreenivasan, B., 2007. Correlation of Earth's magnetic field with lower mantle thermal and seismic structure. Phys. Earth Planet. Inter. 162, 256–260.

Hernlund, J.W., McNamara, A.K., 2015. 7.11 - the core-mantle boundary region. In: Schubert, G. (Ed.), Treatise on Geophysics, second ed. Elsevier, Oxford, pp. 461–519.

Hernlund, J.W., Tackley, P.J., 2008. Modeling mantle convection in the spherical annulus. Phys. Earth Planet. Inter. 171, 48–54.

Hernlund, J.W., Thomas, C., Tackley, P.J., 2005. A doubling of the post-perovskite phase boundary and structure of the Earth's lowermost mantle. Nature 434, 882–886.

Houser, C., Masters, G., Shearer, P., Laske, G., 2008. Shear and compressional velocity models of the mantle from cluster analysis of long-period waveforms. Geophys. J. Int. 174, 195–212.

Hsieh, W.-P., Deschamps, F., Okuchi, T., Lin, J.-F., 2017. Reduced lattice thermal conductivity of fe-bearing bridgmanite in earth's deep mantle. J. Geophys. Res. 122 (7), 4900–4917.

Hsieh, W.-P., Deschamps, F., Okuchi, T., Lin, J.-F., 2018. Effects of iron on the lattice thermal conductivity of earth's deep mantle and implications for mantle dynamics. P. Nat. Acad. Sci. USA 115 (16), 4099–4104.

Irving, J.C., Cottaar, S., Lekić, V., 2018. Seismically determined elastic parameters for earth's outer core. Sci. Adv. 4 (6), eaar2538.

Ishii, M., Tromp, J., 1999. Normal-mode and free-air gravity constraints on lateral variations in velocity and density of earth's mantle. Science 285 (5431), 1231–1236.

Jones, T.D., Maguire, R.R., van Keken, P.E., Ritsema, J., Koelemeijer, P., 2020. Subducted oceanic crust as the origin of seismically slow lower-mantle structures. Prog. Earth Plan. Sci. 7, 1–16.

Kaneshima, S., 2018. Array analyses of smks waves and the stratification of earth's outermost core. Phys. Earth Planet. Inter. 276, 234–246.

Kavner, A., Rainey, E.S., 2016. Heat transfer in the core and mantle. Deep Earth: Physics and Chemistry of the Lower Mantle and Core, pp. 31–42.

Keppler, H., Dubrovinsky, L.S., Narygina, O., Kantor, I., 2008. Optical absorption and radiative thermal conductivity of silicate perovskite to 125 gigapascals. Science 322 (5907), 1529–1532.

Klemens, P., White, G., Tainsh, R., 1962. Scattering of lattice waves by point defects. Philos. Mag. 7 (80), 1323–1335.

Kutzner, C., Christensen, U.R., 2004. Simulated geomagnetic reversals and preferred virtual geomagnetic pole paths. Geophys. J. Int. 157, 1105–1118.

Lau, H.C., Mitrovica, J.X., Davis, J.L., Tromp, J., Yang, H.-Y., Al-Attar, D., 2017. Tidal tomography constrains earth's deep-mantle buoyancy. Nature 551 (7680), 321–326.

Lay, T., Hernlund, J., Buffet, B.A., 2008. Core-mantle boundary heat flow. Nature 1, 25–32.

Lekic, V., Cottaar, S., Dziewonski, A., Romanowicz, B., 2012. Cluster analysis of global lower mantle tomography: A new class of structure and implications for chemical heterogeneity. Earth Planet. Sci. Lett. 357, 68–77.

Li, Y., Deschamps, F., Tackley, P.J., 2016. Small post-perovskite patches at the base of lower mantle primordial reservoirs: Insights from 2-d numerical modeling and implications for ulvzs. Geophys. Res. Lett. 43 (7), 3215–3225.

Li, Y., Deschamps, F., Tackley, P.J., 2014. The stability and structure of primordial reservoirs in the lower mantle: insights from models of thermochemical convection in three-dimensional spherical geometry. Geophys. J. Int. 199 (2), 914–930.

Li, Y., Deschamps, F., Tackley, P.J., 2015. Effects of the post-perovskite phase transition properties on the stability and structure of primordial reservoirs in the lower mantle of the earth. Earth Planet. Sci. Lett. 432, 1–12.

Manthilake, G.M., de Koker, N., Frost, D.J., McCammon, C.A., 2011. Lattice thermal conductivity of lower mantle minerals and heat flux from earth's core. P. Nat. Acad. Sci. USA 108 (44), 17901–17904.

Mao, W.L., Mao, H.-K., Sturhahn, W., Zhao, J., Prakapenka, V.B., Meng, Y., Shu, J., Fei, Y., Hemley, R.J., 2006. Iron-rich post-perovskite and the origin of ultralow-velocity zones. Science 312 (5773), 564–565.

Masters, G., Laske, G., Bolton, H., Dziewonski, A., 2000. The relative behavior of shear velocity, bulk sound velocity, and compressional velocity in the mantle: Implications for chemical and thermal structure. In: Karato, S., Forte, A., Liebermann, R., Masters, G., Stixrude, L. (Eds.), Earth's deep interior, vol. 117. AGU Geophysical Monograph, pp. 63–87.

McNamara, A.K., Zhong, S., 2005. Thermochemical structures beneath Africa and the Pacific Ocean. Nature 437, 1136–1139.

Mosca, I., Cobden, L., Deuss, A., Ritsema, J., Trampert, J., 2012. Seismic and mineralogical structures of the lower mantle from probabilistic tomography. J. Geophys. Res. 117, 6304.

Moulik, P., Ekström, G., 2016. The relationships between large-scale variations in shear velocity, density, and compressional velocity in the earth's mantle. J. Geophys. Res. 121 (4), 2737–2771.

Nakagawa, T., Tackley, P.J., 2008. Lateral variations in CMB heat flux and deep mantle seismic velocity caused by a thermal chemical-phase boundary layer in 3D spherical convection. Earth Planet. Sci. Lett. 271, 348–358.

Ni, S., Tan, E., Gurnis, M., Helmberger, D., 2002. Sharp Sides to the African Superplume. Science 296, 1850–1852.

Ohta, K., Yagi, T., Hirose, K., Ohishi, Y., 2017. Thermal conductivity of ferropericlase in the earth's lower mantle. Earth Planet. Sci. Lett. 465, 29–37.

Ohta, K., Yagi, T., Taketoshi, N., Hirose, K., Komabayashi, T., Baba, T., Ohishi, Y., Hernlund, J., 2012. Lattice thermal conductivity of mgsio3 perovskite and post-perovskite at the core–mantle boundary. Earth Planet. Sci. Lett. 349, 109–115.

Olson, P.L., Christensen, U.R., 2002. The time-averaged magnetic field in numerical dynamos with non-uniform boundary heat flow. Geophys. J. Int. 151, 809–823.

Olson, P.L., Coe, R.S., Driscoll, P.E., Glatzmaier, G.A., Roberts, P.H., 2010. Geodynamo reversal frequency and heterogeneous core-mantle boundary heat flow. Phys. Earth Planet. Inter. 180, 66–79.

Olson, P.L., Deguen, R., Rudolph, M.L., Zhong, S., 2015. Core evolution driven by mantle global circulation. Phys. Earth Planet. Inter. 243, 44–55.

Sahoo, S., Sreenivasan, B., 2020. Response of Earth's magnetic field to large lower mantle heterogeneity. Earth Planet. Sci. Lett. 549, 116507.

Tackley, P.J., 2008. Modelling compressible mantle convection with large viscosity contrasts in a three-dimensional spherical shell using the yin-yang grid. Phys. Earth Planet. Inter. 171, 7–18.

Tackley, P.J., 2012. Dynamics and evolution of the deep mantle resulting from thermal, chemical, phase and melting effects. Earth Sci. Rev. 110, 1–25.

Tarduno, J., Watkeys, M., Huffman, T., Cottrell, D., Blackman, E., Wendt, A., Scribner, A., Wagner, C., 2015. Antiquity of the South Atantic Anomaly and evidence for top-down control on the geodynamo. Nat. Commun. 6, 7865. https://doi.org/10.1038/ncomms8865.

Terra-Nova, F., Amit, H., Choblet, G., 2019. Preferred locations of weak surface field in numerical dynamos with heterogeneous core-mantle boundary heat flux: Consequences for the south atlantic anomaly. Geophys. J. Int.

Terra-Nova, F., Amit, H., Hartmann, G.A., Trindade, R.I.F., 2016. Using archaeomagnetic field models to constrain the physics of the core: robustness and preferred locations of reversed flux patches. Geophys. J. Int. 206, 1890–1913.

Trampert, J., Deschamps, F., Resovsky, J., Yuen, D., 2004. Probabilistic tomography maps chemical heterogenities throughout the mantle. Science 306, 853–856.

Vilella, K., Bodin, T., Boukaré, C.-E., Deschamps, F., Badro, J., Ballmer, M., Li, Y., 2020. Constraints on the composition and temperature of llsvps from seismic properties of lower mantle minerals. Earth Planet. Sci. Lett. 554, 116685.

Workman, R.K., Hart, S.R., 2005. Major and trace element composition of the depleted morb mantle (dmm). Earth Planet. Sci. Lett. 231 (1–2), 53–72.

Yang, H.-Y., Tromp, J., 2015. Synthetic free-oscillation spectra: an appraisal of various mode-coupling methods. Geophys. J. Int. 203 (2), 1179–1192.

Yoshimura, Y., 2022. The cretaceous normal superchron: a mini-review of its discovery, short reversal events, paleointensity, paleosecular variations, paleoenvironment, volcanism, and mechanism. Front. Earth Sci. 10, 834024.

Yu, S., Garnero, E.J., 2018. Ultralow velocity zone locations: A global assessment. Geochem. Geophys. Geosyst. 19 (2), 396–414.